Structural, magnetic, optical, and photocatalytic properties of Ca–Ni doped BiFeO$_3$ nanoparticles

Babita Tripathi[1], Sunil Chauhan[1,*] , Manoj Kumar[2], Mohit Sahni[1], Pankaj Gupta[3], Prakash Chand Sati[4], Satyendra Singh[5], Daksh Agarwal[6], and R. C. Singh[1]

[1] Department of Physics, Centre of Excellence in Solar Cell and Renewable Energy, SBSR, Sharda University, Greater Noida, U. P. 201310, India

[2] Department of Physics and Materials Science, JIIT Noida, Noida, U. P. 201309, India

[3] Department of Chemistry and Biochemistry, SBSR, Sharda University, Greater Noida, U. P. 201310, India

[4] Department of Physics, Rajiv Gandhi Government Post Graduate College, Mandsaur, Madhya Pradesh 458001, India

[5] Special Centre for Nanoscience, Jawaharlal Nehru University, New Delhi 110067, India

[6] Department of Materials Science and Engineering, University of Pennsylvania, Philadelphia, PA 19104, USA

ABSTRACT

In this article, we have studied the structural, magnetic, optical, and photocatalytic properties of Bi$_{1-x}$Ca$_x$Fe$_{1-x}$Ni$_x$O$_3$ multiferroics synthesized by sol–gel method. X-ray diffraction predicted the superposition of two structural phases (rhombohedral-*R3c* + orthorhombic-*Pnma*) for (x = 0.05, 0.10) samples. Correspondingly, drastic variations in the Raman modes were detected at low and high wavenumbers with increasing the Ca–Ni content. The larger change in the magnetic parameters at room temperature was identified for Bi$_{0.90}$Ca$_{0.10}$Fe$_{0.90}$Ni$_{0.10}$O$_3$ nanoparticles caused by the formation of a new orthorhombic phase. The XPS spectroscopy study supported the magnetic enhancement in x = 0.10 samples due to increasing concentration of Fe^{2+}, Ni^{2+} ions, and oxygen vacancies. The shift of ESR pattern with doping agrees with the magnetization values. The energy band gap values were altered by increasing the Ca–Ni content in BiFeO$_3$ samples, from 2.22 to 2.05 eV. The photocatalytic activity of Ca–Ni doped BiFeO$_3$ photocatalyst showed higher degradation rate (− 0.035/min) of Methylene blue (MB) in comparison to pure BiFeO$_3$.

1 Introduction

Multiferroicity is the nature of existence of more than two ferroic orders out of the following viz., ferroelectric, ferromagnetic, and ferro elastic in a single phase of material. Such types of materials are called multiferroic materials [1–3]. Recently, multiferroics are giving rise to the possibilities for electric-field control of magnetization in such a way that these materials do have the potential applications for spintronics, data storage, and high-frequency

---

Address correspondence to E-mail: sunil.chauhan@sharda.ac.in

magnetic devices [4, 5]. The grand challenges in multiferroics are to design it with enhanced magnetic, ferroelectric, and optical properties. Bismuth ferrite ($BiFeO_3$) (BFO) is a novel single phase multiferroic compound, having ferroelectric transition temperature $T_C \sim 1103$ K and antiferromagnetic transition temperature $T_N \sim 643$ K [6, 7]. BFO is characterized by strong coupling feature between its ferroelectric and antiferromagnetic ordering. The multiferroic materials are an integral need for multiple device applications to serve in the premises of spintronics, LEDs, and magnetic recording systems [8, 9]. Currently, $BiFeO_3$ has also become popular as a source of best photocatalyst under UV–visible range and piezo-catalyst due to its lower band gap which is near about 2.1 eV, its stability and electrically polarized nature [10–12]. Besides all these characteristics, industrial applications of $BiFeO_3$ are still very less due to its large charge (e^- and h^+) recombination rate within lattices of particles [11–13]. To find out the best result, several strategies have been reported by previous articles like single or co-doping of rare earth elements, formation of composite heterostructure, and by using different synthesis methods [14–16]. Single or co-doping of rare earth elements with $BiFeO_3$ is widely treated as a best way to boost the magnetic, optical, and photocatalytic performance [17, 18]. The dopant-elements work as the charge trapping sites within the lattice of $BiFeO_3$, it improves the movement of charges from one carrier to another carrier and reduces their recombination rate [19–21]. Usually, the needful substitution of dopants, in limited concentration, can influence the modification of structural, magnetic, optical, and photocatalytic nature of $BiFeO_3$. The semiconductor $BiFeO_3$ nanoparticles, when excited by light under different UV–visible wavelengths, the lower band gap actively participates in photocatalytic activities [22–24]. The activated ions and super radicals present in photocatalyst helps in decontamination of organic, inorganic, bacterial, and microbial pollutants from contaminated water [25, 26]. As a result of this, huge work has been carried out in the field of Bi-based photocatalytic materials for the application of purification of water in recent decades [27–29]. Presently, this work focuses on the observed effects of co-doping of Ca–Ni on the structural, magnetic, optical, and photocatalytic properties of $BiFeO_3$ nanoparticles synthesized via the sol–gel technique that have been explored in detail here. Rietveld refinement of the

XRD pattern result indicates that, with increasing Ca–Ni amount in $BiFeO_3$ from $x = 5$–10%, the R3c phases decrease while $Pnma$ phase increases correspondingly. The TEM images show that the particle size of the considered samples is in the nano-range, which is observed to decrease as Ca and Ni content rises in $BiFeO_3$. The Raman modes conform to the result of XRD and show structural variation from $R3c$ phase to $Pnma$ phase. The M-H loop and ESR results suggest the presence of strong ferromagnetic nature in Ca-Ni doped $BiFeO_3$ in comparison to pristine BFO. XPS study supported the magnetization enhancement in $x = 0.10$ samples due to increasing concentration of Fe^{2+}, Ni^{2+} ions, and oxygen vacancies. The optical properties are analysed by using UV–visible absorption spectra which confirm the alteration of band gap of $Bi_{1-x}Ca_xFe_{1-x}Ni_xO_3$ nanoparticles from 2.2 to 2.05 eV with Ca–Ni content. The change in band gap improves the photocatalytic activity, also the appreciable MB dye degradation 98.36% in 160 min irradiation under UV-light is observed using $Bi_{1-x}Ca_xFe_{1-x}Ni_xO_3$ ($x = 0.10$) photocatalyst.

2 Experimental details

2.1 Photocatalyst synthesis

In the synthesis of $Bi_{1-x}Ca_xFe_{1-x}Ni_xO_3$ nanoparticles, the chemical reagents $Bi(NO_3)_3.5H_2O$ ($\geq 98\%$), $Fe(NO_3)_3.9H_2O$ ($\geq 98\%$), $Ca(NO_3)_2$ ($\geq 98\%$), $Ni(NO_3)_2.6H_2O$ ($\geq 99.9\%$); Tartaric Acid ($\geq 99.0\%$) and Nitric acid were used. All the chemical (Sigma) reagents used were of analytic grade and do not require additional purification treatment. $Bi_{1-x}Ca_xFe_{1-x}Ni_xO_3$ ($x = 0.0, 0.05, 0.10$) multiferroic nanoparticles (NPs) were synthesized by sol–gel method using chelating reagent tartaric acid [18]. The schematic flow-chart of the synthesis of $Bi_{1-x}Ca_xFe_{1-x}Ni_xO_3$ nanoparticles is shown in the Fig. 1. The calculated amount of $Bi(NO_3)_3.5H_2O$ mixed in deionized water and the transparent solution was obtained by adding the 15 ml of dilute nitric acid. After this the calculated amount of $Fe(NO_3)_3.9H_2O$ were added. For the complete combustion of the nitrates stoichiometric amount of tartaric acid was added to the transparent solution. The transparent light yellow coloured solution was stirred upon hot plate at 60 °C for 24 h. This transparent mixture solution was kept on 60–80 °C with

continuous stirring till fluffy gel was obtained. The dried samples were calcined at 600 °C for 2 h in an air ambience. After the calcination, sample was ground with the help of mortal pastel to get the powder form of material for further characterization. The similar process was used in all $Bi_{1-x}Ca_xFe_{1-x}Ni_xO_3$ ($x = 0.05, 0.10$) samples, only the calculated amount of dopants, calcium nitrate and nickel nitrate were added in the precursor solution. All other synthesis conditions were kept unchanged.

2.2 Characterizations

The prepared samples were characterized structurally by using Shimadzu 600 XRD. TECNAI 200 kV TEM Fei along with Electron Optics was used in order to analyse the morphology of the samples. The backscattering configuration was used while performing Raman spectroscopy with LabRAM HR spectrometer. The magnetic resonance spectra were gathered by adopting JES FA200 CW ESR Spectrometer, using X-band gun diode. The measurements for magnetism of the samples were identified with the assistance of Lakeshore VSM 7410. The optical and photocatalytic properties of the synthesized samples were analysed by using LABMAN-

900S UV–visible spectrometer. To find out the photocatalytic degradation of MB dye, a 250 W Hg bulb was kept in water circulating jar placed in quartz container (500 ml) at constant temperature (below 10 °C) with continuous stirring. For observation of dye diminishment with time under UV–Visible light, equal amount of samples were collected and after centrifugal process, all samples were passed through UV–visible absorbance spectra to find out their MB dye degradation efficiency comparative data.

3 Result and discussion

3.1 X-ray diffraction, SEM and TEM analysis

The X-ray diffraction peaks of the sol–gel synthesized $BiFeO_3$ (BFO), $Bi_{0.95}Ca_{0.05}Fe_{0.95}Ni_{0.05}O_3$, $Bi_{0.90}Ca_{0.10}Fe_{0.90}Ni_{0.10}O_3$, and $Bi_{0.85}Ca_{0.15}Fe_{0.85}Ni_{0.15}O_3$ samples are displayed in Fig. 2. All peaks in pure BFO diffraction pattern can be labelled with the R3c space group as per the distorted rhombohedral structure (JCPDS file no. 71–2494) [18]. The diffraction pattern shifted towards higher angles leading to the unit cell contraction in BFO when the Ca-Ni were partially

Fig. 1 The schematic diagram of synthesis of multiferroic $Bi_{1-x}Ca_xFe_{1-x}Ni_xO_3$ nanoparticles
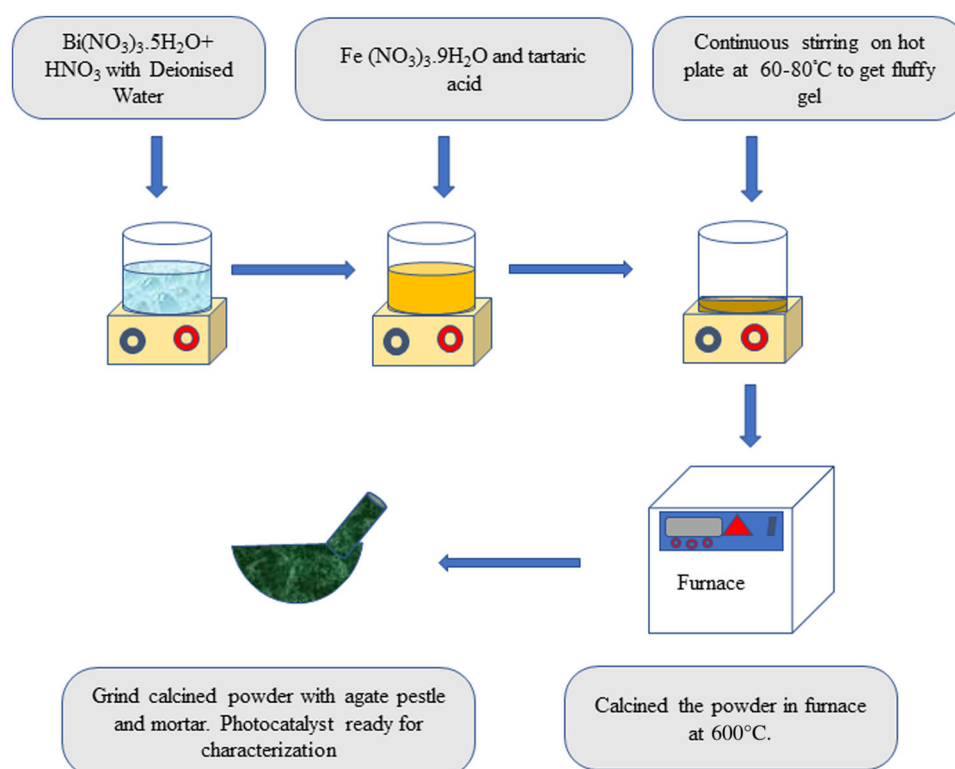
doped on Bi and Fe site correspondingly. The intense, sharp nature diffraction peaks are indicating the samples' high crystalline properties. The nonappearance of any other peak indicated the phase purity of the synthesized $x = 0.00$, 0.05, & 0.10 samples within the XRD limitations. However, XRD pattern of $Bi_{0.85}Ca_{0.15}Fe_{0.85}Ni_{0.15}O_3$ shows the large impurity phase corresponding to ferrite.

Phase formation and crystal structure of the pure and Ca–Ni substituted $BiFeO_3$ nanoparticles were further analized by Rietveld refinement of their XRD patterns adopting FULLPROF software as shown in Fig. 3a–c. The Rietveld analysis showed pure BFO exhibited rhombohedral structure with $R3c$ space, while co-doped samples showed co-existence of rhombohedral and orthorhombic structure with $R3c$ and $Pnma$ space group, respectively. Although, with increasing Ca–Ni amount in pure $BiFeO_3$ from $x = 5$–10%, the presence of R3c decreases while $Pnma$ phase fraction progressively increases as shown in Table 1. Moreover, increasing Ca–Ni concentration leads to the evolution of peaks related to the Pnma phase. Such severe changes in XRD pattern indicates that the Ca–Ni co-doped at Bi-site and Fe- site of BFO correspondingly, suppress and merges the sharp diffraction peak (110) and (104) related to R3c phase in the doped samples in order to get single diffraction peak related to Pnma phase. This is confirmed from

Rietveld analysis. It also indicates that co-dopant change the crystalline nature of solid solution to nanocrystalline via gradual enhancement in the broadening of diffraction peaks with increasing doping. From Rietveld analysis, the lattice parameter values, fraction values of phases, atomic position coordinate values, and R-factors of both phases were also obtained and are summarized in Table 1. The observed and calculated XRD patterns showed compatible results. The values of scale-factor, unit cell parameters (a, b, c), elemental positions (x, y, z), half-width values (U, V, W), thermal and background parameters were changed, whereas the elemental occupancy remained same during whole refinement processes. The peak fitting and background correction have been performed by adopting Pseudo-Voigt function with linear interpolation method correspondingly [30–32]. The estimated structural refinement results were summarized in Table 1. The average crystallite size of the synthesized nanocrystalline $Bi_{1-x}Ca_xFe_{1-x}Ni_xO_3$ samples was found with the assistance of Scherrer's formula.

$$D = \frac{K\lambda}{\beta_{hkl}Cos(\Theta_{hkl})}$$

where symbol D represents crystalline size, symbols K and λ denotes the shape-factor (0.9) and wavelength of Cu k_α XRD radiation (1.54 Å), respectively.

Fig. 2 a XRD patterns of $Bi_{1-x}Ca_xFe_{1-x}Ni_xO_3$, $x = 0.00$, 0.05, 0.10, and 0.15 nanoparticles with enlarged view around (104) and (110) peaks in (**b**)
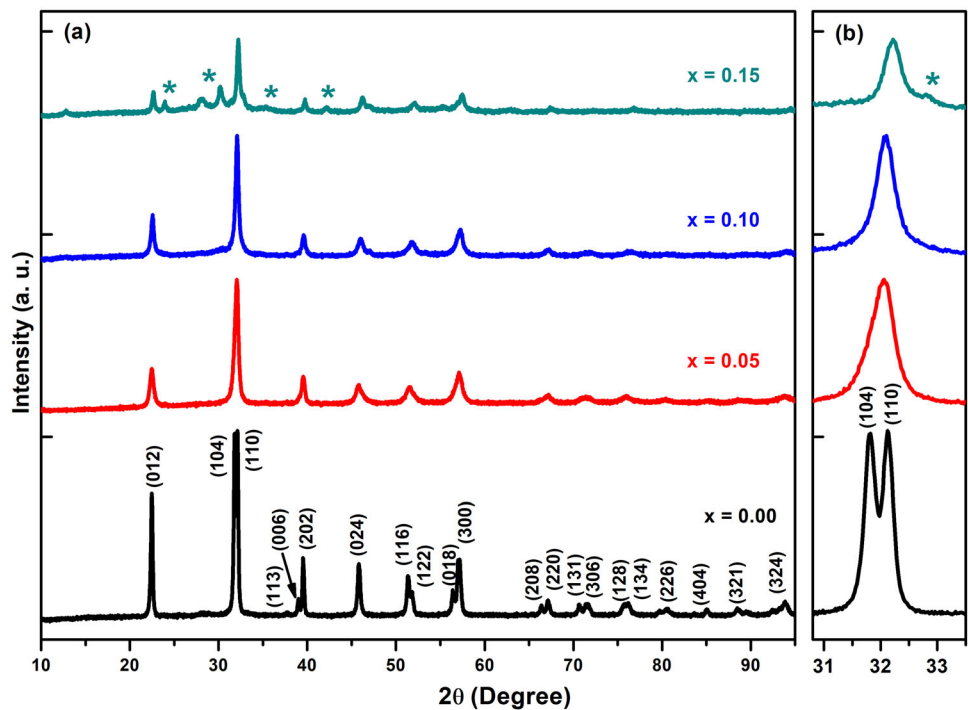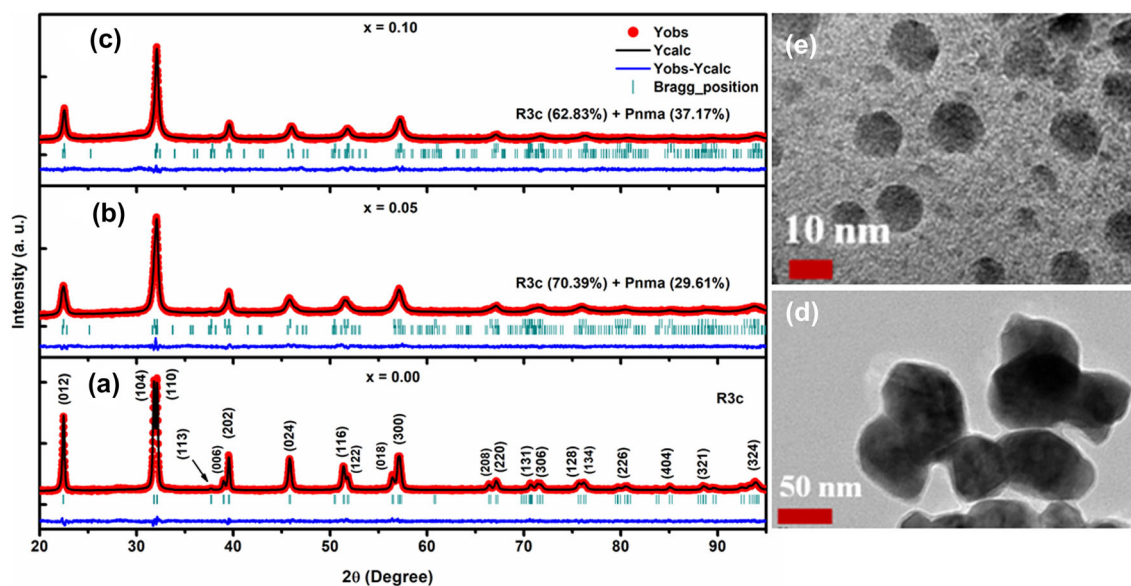
Fig. 3 Rietveld refinement XRD patterns of $Bi_{1-x}Ca_xFe_{1-x}Ni_xO_3$, **a** $x = 0.00$, **b** $x = 0.05$ and **c** $x = 0.10$. TEM images of $Bi_{1-x}Ca_xFe_{1-x}Ni_xO_3$ nanoparticles, **d** $x = 0.00$ and **e** $x = 0.10$

Table 1 Rietveld refined structural parameters of $Bi_{1-x}Ca_xFe_{1-x}Ni_xO_3$ nanoparticles with $x = 0.0, 0.05$, and 0.10

Sample name	Crystal structure	Lattice parameters	Atomic coordinates	R-factors (%)
	Rhombohedral ($R3c$)	$a = 5.5751$ Å	Bi (0, 0, 0.0190)	$R_p = 2.49$, $R_{wp} = 3.17$, $\chi^2 = 1.6$
$x = 0.0$		$c = 13.8590$ Å	Fe (0, 0, 0.29745)	$R_{Bragg} = 1.17$, $R_f = 1.75$
	Crystallite size 82 nm	$V = 373.061$ Å^3	O (0.2307, 0.3581, 0.0833)	
$x = 0.05$	Rhombohedral ($R3c$)	$a = 5.5767$ Å	Bi/Ca (0, 0, 0.2037)	$R_p = 3.00$, $R_{wp} = 3.76$, $\chi^2 = 1.50$
	(69.39%)	$c = 13.8168$ Å	Fe/Ni (0, 0, -0.0172)	
		$V = 372.1306$ Å^3	O (0.2087, 0.3313, 0.0833)	$R_{Bragg1} = 2.17$, $R_{f1} = 1.54$
	Orthorhombic ($Pnma$)	$a = 5.6556$ Å	Bi/Ca (0.0122, 0.25, 0.9811)	$R_{Bragg2} = 3.97$, $R_{f2} = 3.49$
	(30.61%)	$b = 7.8023$ Å	Fe/Ni (0, 0, 0.5)	
		$c = 5.5983$ Å	O_1 (0.3164, 0.25, 0.1910)	
		$V = 247.0341$ Å^3	O_2 (0.1652, 0.5299, 0.2474)	
$x = 0.10$	Rhombohedral ($R3c$)	$a = 5.5730$ Å	Bi/Ca (0, 0, 0.2105)	$R_p = 2.84$, $R_{wp} = 3.58$, $\chi^2 = 1.49$
	(62.83%)	$c = 13.700$ Å	Fe/Ni (0, 0, -0.0106)	
	Crystallite size 47 nm	$V = 368.4930$ Å^3	O (0.2281, 0.3193, 0.0833)	$R_{Bragg1} = 2.00$, $R_{f1} = 1.82$
	Orthorhombic ($Pnma$)	$a = 5.6052$ Å	Bi/Ca (0.01376, 0.25, 0.99555)	$R_{Bragg2} = 3.55$, $R_{f2} = 3.69$
	(37.17%)	$b = 7.9455$ Å	Fe/Ni (0, 0, 0.5)	
	Crystallite size 32 nm	$c = 5.5257$ Å	O_1 (0.3217, 0.25, 0.1967)	
		$V = 246.0945$Å^3	O_2 (0.2051, 0.5627, 0.2617)	

The β_{hkl} refers to Full Width at Half Maxima (FWHM) parameters used during Rietveld refinement of XRD patterns. In accord to Rietveld method, the different parameters to the FWHM from diffraction patterns can be identified using the equation,

$$FWHM^2 = (U + D_{ST}^2)(\tan^2\theta) + V(\tan\theta) + W + \frac{IG}{\cos^2\theta}$$

Here U, V, W represent the shape parameters of the peaks. IG for isotropic size effect and D_{ST} represents strain—coefficient. The crystallite size and their lattice parameters for the $Bi_{1-x}Na_xFe_{1-x}Co_xO_3$ samples are presented in Table 1. The decrease in the crystalline size was observed with higher Ca–Ni doping in pure $BiFeO_3$ nanocrystals. This could be achieved

because of the ion size disparity between the host and the doped ions leads to lattice strain. This lattice strain also introduced local structural distortion causing acceleration in the nucleation rate, leading to a reduction in crystallite size. The TEM and HRTEM micrographs of Ca–Ni doped $BiFeO_3$ nanoparticles are represented in Fig. 3e, f and Fig. S2. It shows a spherical particle with a nanosized of about 50–90 nm range for pure BFO sample and 10–30 nm range for 10% (Ca–Ni) doped sample. The TEM result shows that the size of nanoparticles is in the nano-range and reduced as Ca–Ni content rises in BFO. The reduction in nanoparticles size due to Ca–Ni doping in $BiFeO_3$ occurs due to presence of lattice induction through ionic radius mismatches. The lattice strains increase the nucleation rate and help in limiting the growth of nanoparticles.

Figure 4a–c represent the SEM micrographs revealing the morphology of the $Bi_{1-x}Ca_xFe_{1-x}Ni_xO_3$ samples. According to these micrographs, the synthesized samples have dense morphology, their grain shapes are spherical, and their sizes are in between 20 and 125 nm. SEM images also demonstrate the decrease in grain size and increased agglomeration with increasing the Ca-Ni content. Grain growth in $Bi_{1-x}Ca_xFe_{1-x}Ni_xO_3$ ($x = 0.05$ and 0.10) nanocrystalline samples is inversely proportional to the rate of nucleation. When rate of nucleation is accelerated by lattice strain in the system, the particle growth decreases.

The Bi, Ca, Fe, Ni, and O elemental mapping of the synthesized samples have been also completed using the EDS in SEM attachment. The elemental mapping of the $Bi_{1-x}Ca_xFe_{1-x}Ni_xO_3$ ($x = 0.00, 0.05$, and 0.10) samples represented in the supplementary information Fig. S1. The chemical composition of pristine $BiFeO_3$ nanoparticles shows evident signals for Bi, Fe,

and O consenting with the nominal ratio, 1: 1: 3, approximately. Moreover, weak signals of Ca and Ni in $x = 0.05$ and $x = 0.10$ compositions have been found in EDS spectra. The measured quantitative atomic percent values are 20.20% Bi, 19.00% Fe, and 60.80% O for $BiFeO_3$ sample; 21.8% Bi, 0.8% Ca, 19.20% Fe, 0.2% Ni, and 58.00% O for $x = 0.05$ sample and 23.2% Bi, 3.2% Ca, 18.24% Fe, 2.8% Ni, and 52.56% O for $x = 0.25$ sample. This indicates that Ca–Ni ions have conveniently been incorporated into the host lattice. Elemental mapping of the $x = 0.05$ and 0.10 samples showed, Ca and Ni are uniformly distributed in the mapping micrograph. No other phase of the Ca and Ni is observed in the mapping micrographs.

3.2 Raman spectroscopy

The Raman scattering spectra of $Bi_{1-x}Ca_xFe_{1-x}Ni_xO_3$ nanoparticles is displayed in Fig. 5a. The peak fitted Raman spectra of $BiFeO_3$ samples is shown in Fig. 5b and for $Bi_{0.95}Ca_{0.05}Fe_{0.95}Ni_{0.05}O_3$, and $Bi_{0.90}Ca_{0.10}Fe_{0.90}Ni_{0.10}O_3$ samples are displayed in Fig. 6a, b, respectively. BFO having rhombohedral R3c symmetry possess 13 optical-phonon active modes ($4A_1 + 9E$) in accord to well-known group theory [33]. As exhibited in Fig. 5a, all the key active modes that emerged in the pure BFO shows well agreement with the mode of the rhombohedral distorted (R3c) perovskite structure. The observed low frequency modes have been consigned to Bi–O vibration, whereas observed high-frequency Raman modes are linked to the stretching and bending of Fe–O [34]. The measured spectrum was fitted by performing decomposition of the curve into discrete Raman active component with a Lorentz type curve and associated peak positions are summarized in Table 2.
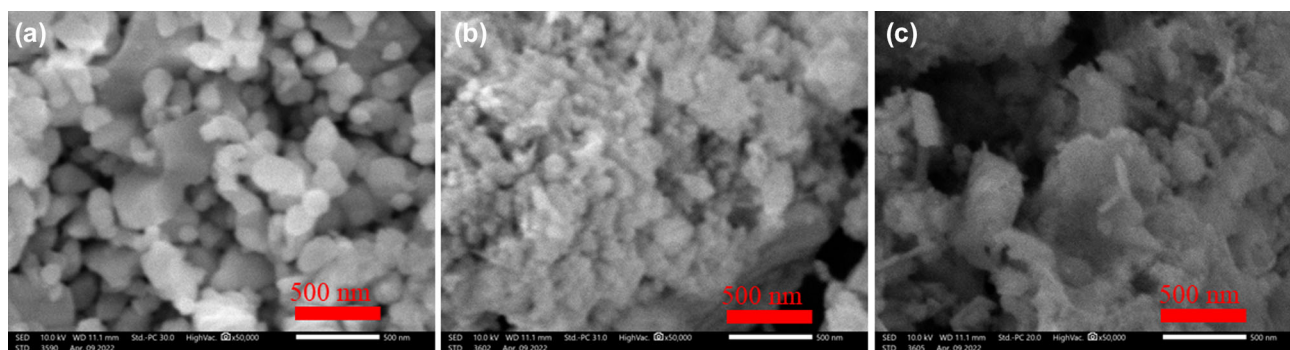
Fig. 4 SEM Micrographs of $Bi_{1-x}Ca_xFe_{1-x}Ni_xO_3$ nanoparticles. **a** $x = 0.0$, **b** $x = 0.05$, and **c** $x = 0.10$
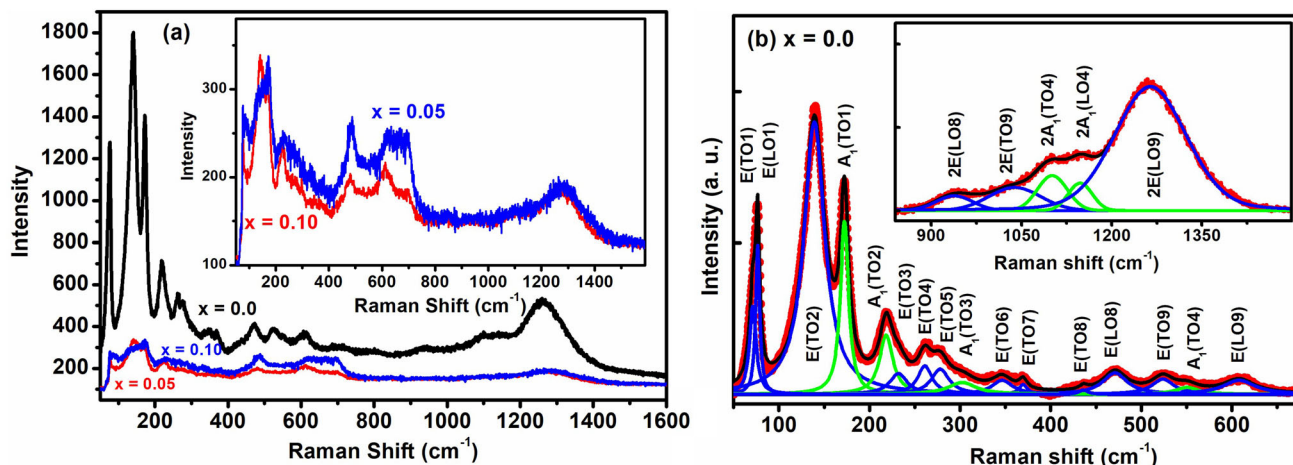
Fig. 5 a Raman spectra of $Bi_{1-x}Ca_xFe_{1-x}Ni_xO_3$ **b** Deconvoluted Raman modes of $BiFeO_3$ nanoparticles in the wavenumber range from 50 to 700 cm^{-1}, **b** the Raman spectra in the range from 800 to 1500 cm.$^{-1}$

Although, doping of Ca–Ni has resulted into few variations in Raman modes of BFO. The first is a clear decrease in the intensity of E(TO2) mode, gradual enhancement in intensity of A1 (TO1) mode, merging of E(TO2) and A_1(TO1) mode. In addition, modes above 400 cm^{-1} that are responsible majorly for variation in magnetic behaviour are boosted for $x = 0.10$ samples. Such severe changes in Raman mode's behaviour strongly suggest structural transformation from parent $R3c$ phase to another $Pnma$ phase.

Moreover, a broad hump in Raman spectra were observed in between 800 and 1500 cm^{-1}, which deconvoluted further into discrete Raman modes identified as two phonons coupling in all samples. The presences of these two phonon modes were linked to the firm spin–lattice interaction between adjoining magnetic sublattices of BFO. These modes represent second over tons of E-modes present between 450 and 700 cm^{-1} and directly related to the magnetic properties of the $BiFeO_3$ nanoparticles [35].

3.3 Magnetic measurements (VSM and ESR)

The room temperature magnetic hysteresis loops (M–H curve) of pure $BiFeO_3$ (BFO), $Bi_{0.95}Ca_{0.05}Fe_{0.95}Ni_{0.05}O_3$, and $Bi_{0.90}Ca_{0.10}Fe_{0.90}Ni_{0.10}O_3$ samples are exhibited in Fig. 7a, the magnified view is shown in Fig. 7b. The M–H curve of pure BFO shows antiferromagnetic (AFM) behaviour with retentivity $M_r = 0.005$ emu/g and maximum magnetization
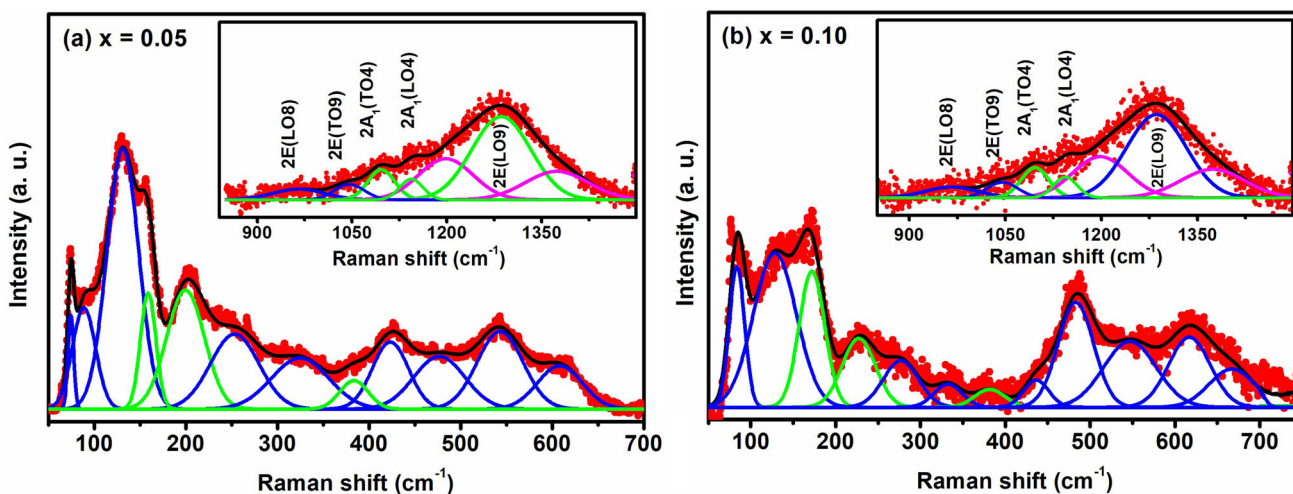
Fig. 6 Deconvoluted Raman modes of $Bi_{1-x}Ca_xFe_{1-x}Ni_xO_3$, **a** $x = 0.05$ and **b** $x = 0.10$

Table 2 Raman modes of $Bi_{1-x}Ca_xFe_{1-x}Ni_xO_3$ nanoparticles with $x = 0.0$, 0.05, and 0.10

Raman modes (cm^{-1})	$x = 0.0$	$x = 0.05$	$x = 0.10$
E(TO1)	71.14	74.4	–
E(LO1)	76.56	88.7	83.6
E(TO2)	139.17	131.2	128.4
A_1(TO1)	172.35	158.9	172.1
A_1(TO2)	218.42	199.7	227.3
E(TO3)	232.19	–	–
E(TO4)	261.21	253.42	–
E(TO5)	278.14	–	277.1
A_1(TO3)	302.41	–	–
E(TO6)	346.56	324.9	332.7
E(TO7)	369.70	383.7	381.9
E(TO8)	436.31	423.4	436.7
E(LO8)	471.17	476.9	483.1
E(TO9)	524.03	–	–
A_1(TO4)	550.84	543.2	547.1
E(LO9)	608.17	608.5	617.2
	–	–	667.4
2E(LO8)	937.06	940	965.8
2E(TO9)	1036.5	140.4	1045.6
2A_1(TO4)	1100.2	1094.8	1096.4
2A_1(LO4)	1147.8	1145.5	1143.7
2E(LO9)	1265.1	1282.2	1286.1
	–	1196.2	1198.3
	–	1369.8	1373.9

M_S = 0.11 emu/g at 15 kOe. While the hysteresis curve of x = 0.05 and 0.10 samples show ferromagnetic behaviour with M_r = 0.0018 emu/g and 0.0078 emu/g and maximum magnetization M_s = 0.37 emu/g and 2.94 emu/g at 15kOe, respectively. Despite the antiferromagnetic nature of BFO, Ca–Ni co-doped samples show ferromagnetic hysteresis loop with enhanced maximum magnetization even at higher magnetic fields (15 kOe). Besides, on comparing magnetization values of pure BFO with co-doped samples, a sensible increase was observed in M_r and M_S of co-doped samples.

To further analyse the magnetic properties of synthesized Ca–Ni substituted $BiFeO_3$ samples, ESR measurement technique has been executed at room temperature, as exhibited in Fig. 7c. The ESR spectra reveals the value of three important factors, asymmetry parameters (Pasy = 1-h_U/h_L, where h_U and h_L denote the absorption peak height), g-factor [$g = hv/\mu_BH_{res}$, where h (Plank constant) is 6.621×10^{-34} Joule-second, μ_B (Bohr

magneton) = 9.2740×10^{-24} JT^{-1}, and H_{res} is Resonance field values of different samples] and ΔB_{p-p} (single width). The magnetic properties of co-doped samples were associated with all these three parameters [36]. The ESR spectra examination calculated g-value (2.05, 2.29, and 2.2), line width (1098, 1160, and 970 Gauss), and asymmetry parameter (0.22, 0.3, and 0.17) with x = 0.0, 0.05, and 0.10 samples, respectively. The degree spin canting values were estimated with the formula $D = (\Delta g/g) J_{super}$ (where symbol D denotes the vector parameters, Δg for deviation value with respect to 2, and J_{super} is a constant value for super exchange coefficient values). The calculated g-factor value was found exceeding 2, specifying the weak ferromagnetic properties in all the samples. The area of the absorption peak, related to the number of excited spins. The area of the absorbance peak increases with increasing the Ca–Ni content, confirm the higher magnetization. The ESR spectra showing the line broadening and shift in resonance peak is attributed to the presence of non-homogenous local magnetic field triggered by the co-existence of Fe–Ni ions in the system.

3.4 X-ray photoelectron spectroscopy (XPS)

To perform analysis of magnetic behaviour, the XPS of the Ca–Ni doped BFO were examined. The XPS narrow scan spectrum of Bi 4f, Fe 2p, Ni 2p, and O1 s are displayed in Fig. 8. The two major characteristic peaks of bismuth centred at 164.1 eV and 158.8 eV, as displayed in Fig. 8a, is attributed to Bi $4f_{5/2}$ and Bi $4f_{7/2}$ correspondingly, which are mainly recognized as a signal from Bi–O bonds [36–40]. The visibility of the two peaks confirms the Bi^{3+} oxidation state in the samples. Spin–orbit intense energy of the Bi 4f doublet is 5.30 eV, which is analogous to the theoretical Spin–orbit splitting energy value of 5.31 eV [37]. Two fitted subpeaks positioned at 158.7 and 164 eV are attributed to Bi ($4f_{7/2}$)–O and Bi ($4f_{5/2}$)–O bonds, whereas other subpeaks positioned at 159.2 and 164.5 eV could be associated to Bi–O–Fe bonds in oxygen octahedron or relaxed Bi phase, possibly created due to cation defects and oxygen vacancies [38, 39].

The $2p_{1/2}$ and $2p_{3/2}$ splitting of Fe 2p core level is shown in Fig. 8b. Broadening of Fe 2p region can be associated to unequal charging of the surface, due to particle's small size [36–40]. The coexistence of two valence state (Fe^{2+} and Fe^{3+}) was affirmed from the

Fig. 7 a M–H curves of $Bi_{1-x}Ca_xFe_{1-x}Ni_xO_3$ nanoparticles. **b** Enlarge view of M–H curves of $Bi_{1-x}Ca_xFe_{1-x}Ni_xO_3$ nanoparticles. **c** ESR spectra of $Bi_{1-x}Ca_xFe_{1-x}Ni_xO_3$, $x = 0.00, 0.05$, and 0.10 nanoparticles
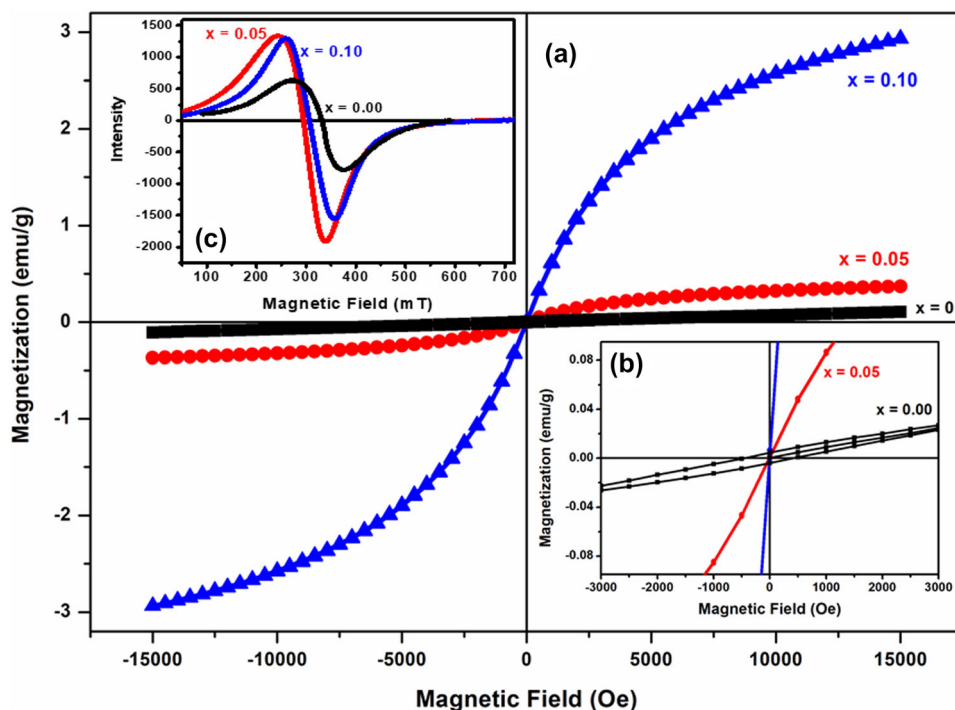

Gaussian deconvolution of the Fe spectra. With well-known energy difference of around 8 eV between $2p_{3/2}$ and $2p_{1/2}$ duplet, Fe2p region was fitted with Fe^{2+} and Fe^{3+} oxidation states [40]. The peaks at 710.50; 725.16 eV for $x = 0.05$ and 710.56, 725.38 eV for $x = 0.10$ can be attributed to Fe^{3+} state of $Fe2p_{3/2}$ and $Fe2p_{1/2}$, whereas the peak at 709.10,723.40 eV for $x = 0.05$ and 709.30, 723.28 eV for $x = 0.10$ is credited to Fe^{2+} in $Fe2p_{1/2}$ and $Fe2p_{3/2}$, respectively. In addition to that, the two-satellite peak was observed at position 718.18 eV, 731.85 eV for $x = 0.05$ and 718.07 eV, 731.33 eV for $x = 0.10$ samples, caused by spin–orbit coupling. The fitting determined the ratio of Fe^{2+}: Fe^{3+} as 0.35 and 0.48 (in $Fe2p_{3/2}$), 0.74 and 0.84 (in $Fe2p_{1/2}$) for $x = 0.05$, and 0.10 samples, respectively, indicating towards increase in quantity of Fe^{2+} ions with increasing Ca–Ni co-doping. The appearance of Fe^{2+} ions contributed a vital part in the boosting of double exchange interaction between Fe^{2+} and Fe^{3+} ions through oxygen, that follow a drastic change in BFO magnetic behaviour from antiferromagnetic to ferromagnetic nature on Ca–Ni co-substitution [41]. The surface peaks situated at 712.7 eV, were observed along with it for $x = 0.05$ and $x = 0.10$ samples that arose owing to reduction in coordination number of Fe^{3+} ions on the surface.

Figure 8c exhibits the XPS spectra of Ni for $x = 0.05$ and $x = 0.10$ samples. In the spectra, the well

separated Ni $2p_{1/2}$ and Ni $2p_{3/2}$ peaks were observed that are further deconvoluted into four peaks with help of peak fit software. The fitted peaks positioned at 873 and 854.5 are associated to Ni^{2+} ions for $x = 0.05$ sample, whilst the peaks positioned at 855.9 and 861.7 are linked to the Fe^{3+} ions and satellite peaks. Similar peaks position for Ni^{2+}, Ni^{3+} ions, and satellite peaks were observed for $x = 0.10$ sample, a slight shift of peak position of the spectra towards lower binding energy. This shift may be owing to increasing distortion in the structure of BFO on increasing co-doping concentration. Hence, XPS analysis predicts about the co-existence of Ni^{2+} and Ni^{3+} ions in co-doped samples with Ni^{2+}/Ni^{3+} ratio of 1.31 and 2.21 for $x = 0.05$ and 0.10 samples, correspondingly. It indicates about higher concentration of Ni^{2+} ions in $x = 0.10$ samples that are responsible for magnetic enhancement.

Figure 8d exhibits the O1s asymmetric spectra of $x = 0.05$ and 0.10 samples. The broad spectra is clearly observable and therefore deconvoluted by fitting three Gaussian peaks. The deconvoluted peaks at a low binding (L.B.) energy 529.4 cm^{-1} ($x = 0.05$) and 529.7 cm^{-1} ($x = 0.10$) attributes to lattice oxygen at normal sites. Whereas other two deconvoluted peaks at middle binding (M.B.) energy 531 cm^{-1} ($x = 0.05$) and 530.8 cm^{-1} ($x = 0.10$) and at high binding (H.B.) energy 532.6 cm^{-1} ($x = 0.05$) and
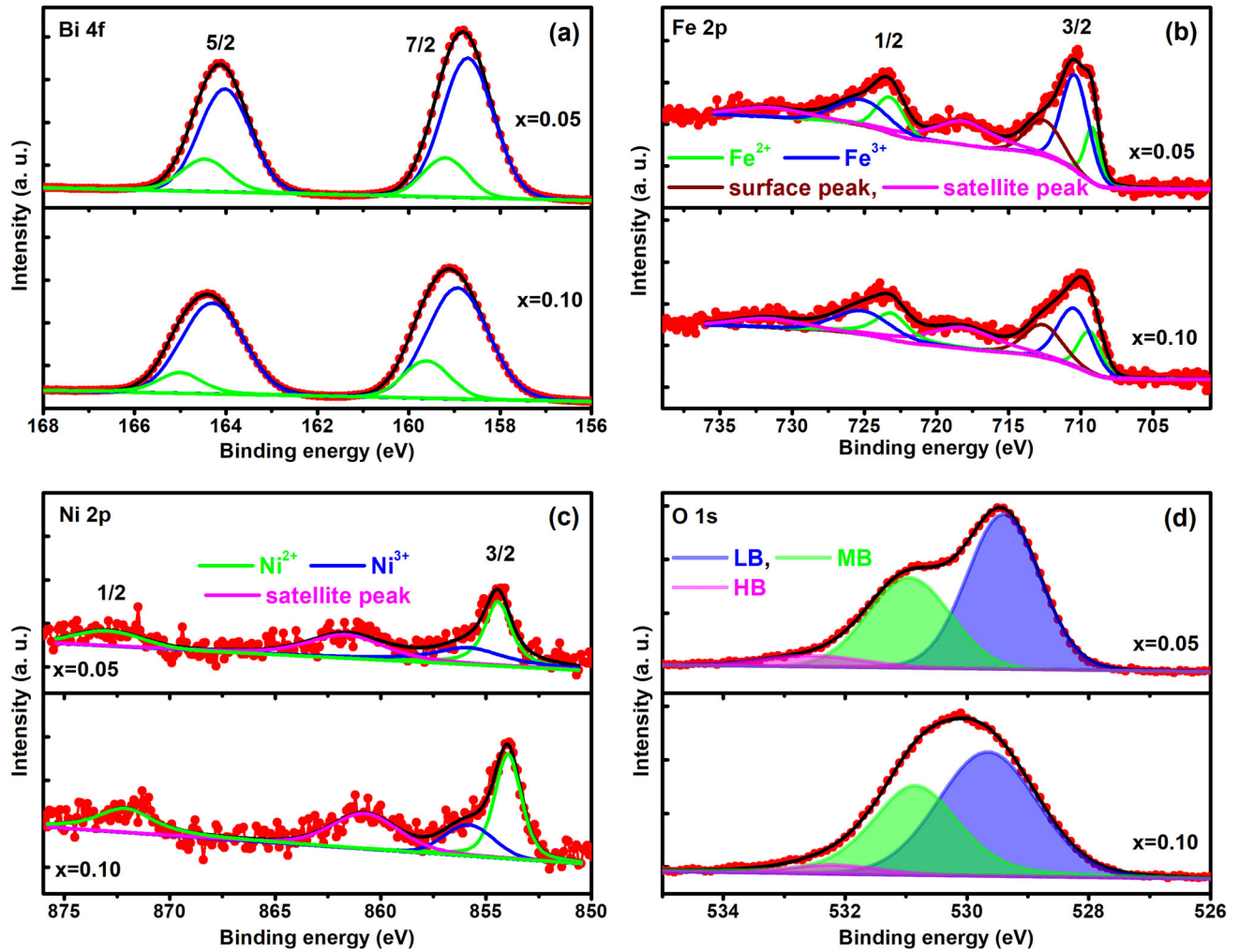
Fig. 8 Deconvoluted core level XPS spectra of **a** Bi 4f, **b** Fe 2p, **c** Ni 2p, and **d** O 1 s lines of $Bi_{1-x}Ca_xFe_{1-x}Ni_xO_3$, x = 0.05 and 0.10 nanoparticles

532.2 cm^{-1} (x = 0.10) are accredited to surface or defect corelated oxygen such as O$^-$, O^{2-} [42]. Although no significant change in the position of deconvoluted peaks occurs with doping, the region under the peak changed significantly as we increased dopant concentration in BFO from x = 0.05 to 0.10. The ratio of the region that comes under the curve of the two peaks (the region of the peak with low binding energy/region of the peak with medium binding energy) can be important because this ratio is precisely related with the concentration of oxygen vacancies. A comparatively large area contribution of the M.B. energy peak for x = 0.10 sturdily advise the occurrence of oxygen vacancies in x = 0.10 in comparison to x = 0.05 sample.

3.5 UV–Visible spectroscopy

The optical properties of nanoparticles depend on their electronic characteristics and bandgaps. These optical properties of pristine $BiFeO_3$, $Bi_{0.95}Ca_{0.05}Fe_{0.95}Ni_{0.05}O_3$, and $Bi_{0.90}Ca_{0.10}Fe_{0.90}Ni_{0.10}O_3$ samples were analysed by UV–Visible absorption spectra displayed in Fig. 9a. The energy bandgap (E_g) was calculated by employing 'Tauc's relation'

$$\alpha = \frac{A(hv - E_g)^{1/2}}{hv}$$

where A refers to a constant, hv refers to photon energy, E_g represents band gap, and α denotes absorption coefficient [41, 42]. The band gap is calculated through the use of Tauc's plot, i.e. $(\alpha hv)^2$ vs hv plot of pristine $BiFeO_3$, $Bi_{0.95}Ca_{0.05}Fe_{0.95}Ni_{0.05}O_3$,

and $Bi_{0.90}Ca_{0.10}Fe_{0.90}Ni_{0.10}O_3$ samples as displayed in Fig. 9b–d. The band gap of pure $BiFeO_3$ is 2.22 eV although after substituting Ca–Ni for $x = 0.05$ and $x = 0.10$ the band gap is diminished from 2.22 to 2.17 eV and 2.2 to 2.05 eV, respectively, displayed in Fig. 9b–d. The substitution of Ca–Ni, results to charge imbalance which indicates the existence of oxygen vacancies in prepared samples. The variation in angle of Fe–O–Fe towards 180° also affects their electronic structure and creates impurity bands. This impurity band enhances charge transfer between the carrier by alteration of energy bandgap [43, 44]. The substitution of Ca–Ni in pristine BFO shows lower energy band gap values, which resulted in improved optical properties of these samples.

3.6 Photocatalytic activity

Photocatalytic effect on MB dye degradation was examined by using $BiFeO_3$, $Bi_{0.95}Ca_{0.05}Fe_{0.95}Ni_{0.05}O_3$, and $Bi_{0.90}Ca_{0.10}Fe_{0.90}Ni_{0.10}O_3$ nano-catalyst under 250Watt mercury vapour lamp. Figure 10a–c shows change in absorbance peak of MB dye in presence of UV–Visible light at different time-intervals. The 10PPM Concentration of MB dye and 0.02 gm mass of photocatalyst was used in photocatalytic reaction. Dye degradation efficiency of Ca–Ni substituted catalysts was calculated by C/Co vs irradiation time graph as given in Fig. 10d, where C and Co refer to final and initial concentration of MB dye during photocatalytic reaction [45, 46]. Graphical analysis revealed that the $Bi_{0.90}Ca_{0.10}Fe_{0.90}Ni_{0.10}O_3$ shows maximum MB degradation, i.e. 98.36% as compare to
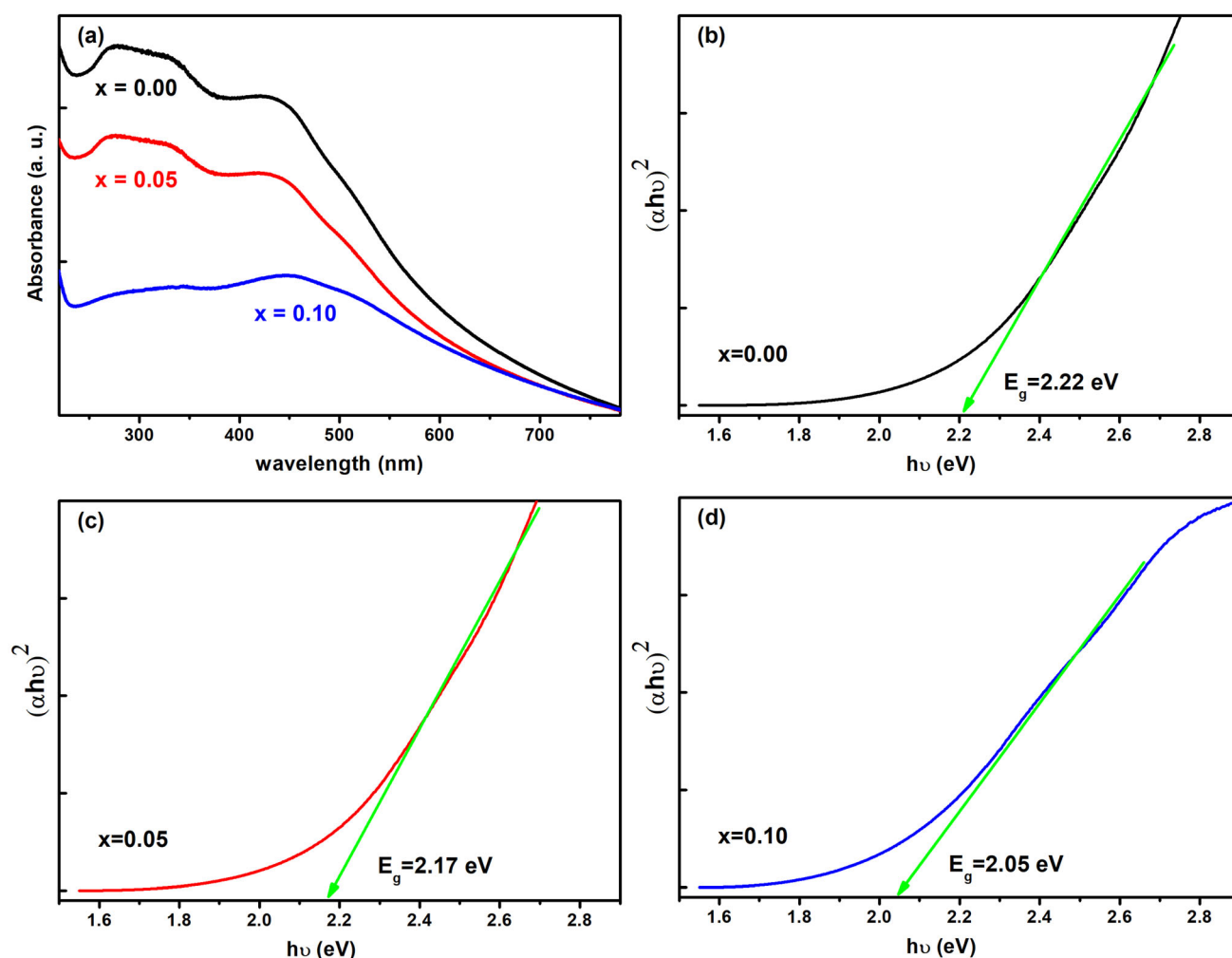
Fig. 9 **a** UV–visible spectra of $Bi_{1-x}Ca_xFe_{1-x}Ni_xO_3$, $x = 0.00$, 0.05, and 0.10 nanoparticles. **b**–**d** Tauc's (($\alpha h\nu$).^{2} vs $h\nu$) plots of $Bi_{1-x}Ca_xFe_{1-x}Ni_xO_3$ nanoparticles

BiFeO$_3$ (96.1%) and Bi$_{0.95}$Ca$_{0.05}$Fe$_{0.95}$Ni$_{0.05}$O$_3$ (95.1%) after equal time observation of 160 min. The rate constant for degradation of the MB dye is determined via usage of Langmuir–Hinshelwood (L–H Model) [47, 48]. L–H model expression is represented by equation given by

$$r = -\frac{dC}{dt} = \frac{K_r KC}{1 + KC}$$

where r refers to degradation rate, K_r refers to rate constant, K refers to equilibrium constant, and C refers to reaction constant. KC is considered as negligible due to less value of C.

So,

$$r = -\frac{dC}{dt} = K_r KC = kC$$

where k (min^{-1}) represents the first order rate constant. At $t = 0$ and $C = C_0$. After entering the values of t and C_0; ln(C/C_0) = kt. The maximum k value is achieved as -0.035 min^{-1} for the Bi$_{0.90}$Ca$_{0.10}$Fe$_{0.90}$Ni$_{0.10}$O$_3$ photocatalyst. Substitution of Ca–Ni in pure BiFeO$_3$ leads to the increment of oxygen vacancies. Due to presence of more free carriers and reduced charge recombination rate, the photocatalytic properties are enhanced in synthesized samples. The interaction of light encouraged electrons and holes on the surface of Ca–Ni substituted BiFeO$_3$ photocatalysts. This absorption process of electron–holes on the surface of photocatalyst leads to redox process where O$_2$ decreases and superoxide anion radical increases, and oxidation process produces hydroxyl radical (OH$^·$) that participate in the decontamination process of MB dye [47]. This process facilitates the
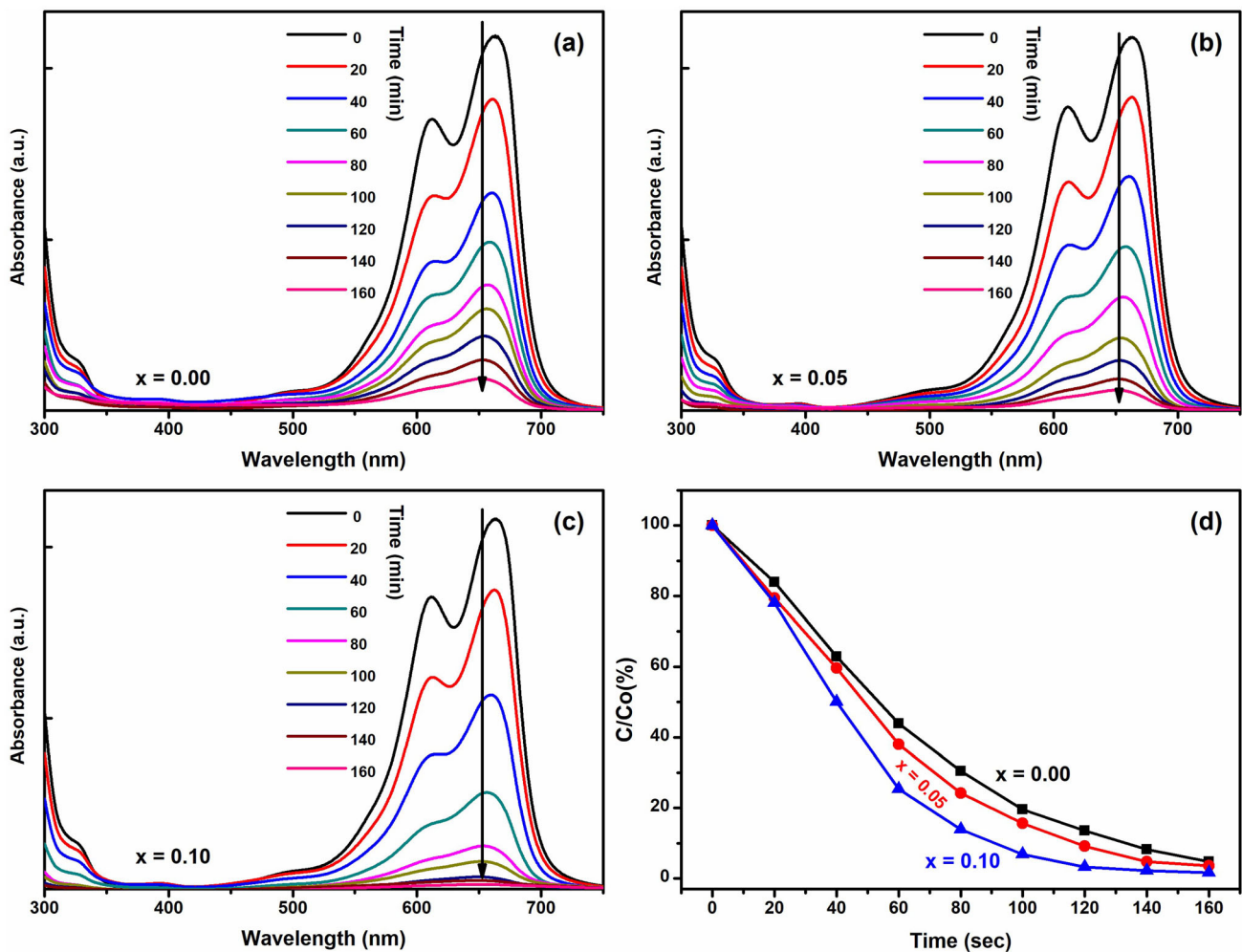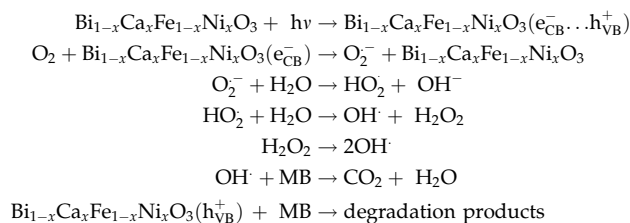

Fig. 10 UV–visible absorption spectra of MB with different irradiation time with Bi$_{1-x}$Ca$_x$Fe$_{1-x}$Ni$_x$O$_3$, **a** $x = 0.00$, **b** $x = 0.05$ **c** $x = 0.10$ nano-photocatalyst. **d** C/C_0 Vs time of MB degradation with Bi$_{1-x}$Ca$_x$Fe$_{1-x}$Ni$_x$O$_3$ nano-photocatalyst

transferring of the electrons and holes to the surface of the photocatalyst. This photocatalytic reaction results into the decontamination of the MB dye and purification of water.

3.7 Mechanism of dye degradation

The photocatalytic dye degradation mechanism has been shown in Fig. 11 with advance oxidation process (AOP). When UV–Visible light was irradiated on the surface of $Bi_{1-x}Ca_xFe_{1-x}Ni_xO_3$ nanomaterials, an excited electron (e^-) moves from VB to CB and produces photoinduced holes (h^+) on the VB sites. Under continuous charge-separation process, e^- and h^+ migrated on the surface of photocatalyst and perform redox reaction with sorbed radicals. The photogenerated holes (h^+) respond with H_2O and produce hydroxyl (OH^-) radicals, whereas electrons (e^-) react with oxygen (O_2) to form superoxide ($O_2^{\cdot-}$) anion radicals. These superoxide radicals ($O_2^{\cdot-}$) combine with holes to form $OH^\cdot$ which is decomposed to OH^- radicals. Lastly, the $OH^\cdot$ participates in oxidation process with MB dye and after reaction CO_2 and H_2O are obtained [49]. The complete photocatalytic mechanism is expressed in the following equations.

$$Bi_{1-x}Ca_xFe_{1-x}Ni_xO_3 + hv \rightarrow Bi_{1-x}Ca_xFe_{1-x}Ni_xO_3(e_{CB}^- \ldots h_{VB}^+)$$
$$O_2 + Bi_{1-x}Ca_xFe_{1-x}Ni_xO_3(e_{CB}^-) \rightarrow O_2^- + Bi_{1-x}Ca_xFe_{1-x}Ni_xO_3$$
$$O_2^- + H_2O \rightarrow HO_2 + OH^-$$
$$HO_2 + H_2O \rightarrow OH^\cdot + H_2O_2$$
$$H_2O_2 \rightarrow 2OH^\cdot$$
$$OH^\cdot + MB \rightarrow CO_2 + H_2O$$
$$Bi_{1-x}Ca_xFe_{1-x}Ni_xO_3(h_{VB}^+) + MB \rightarrow degradation\ products$$

This improved photocatalytic activity due to increases charge carrier transfer and decreases charge recombination rate [50, 51]. The $Bi_{0.90}Ca_{0.10}Fe_{0.90}Ni_{0.10}O_3$ photocatalyst was found as the best dye degradation nanomaterial for degradation of MB Dye. To illustrate the mechanism of photodegradation, the trapping experiment provided the precise results to find the role and responsibility of active species [52]. The scavenger radicals helped to find out further explanation of mechanism of photocatalytic MB dye diminishment from water in the presence of UV–visible light.

To imitate the mechanism of photocatalytic reaction for the degradation of MB dye, the experiment was performed in the presence as well as absence of active species scavengers' reagents. There were two

Fig. 11 Mechanism of photocatalytic degradation of MB dye
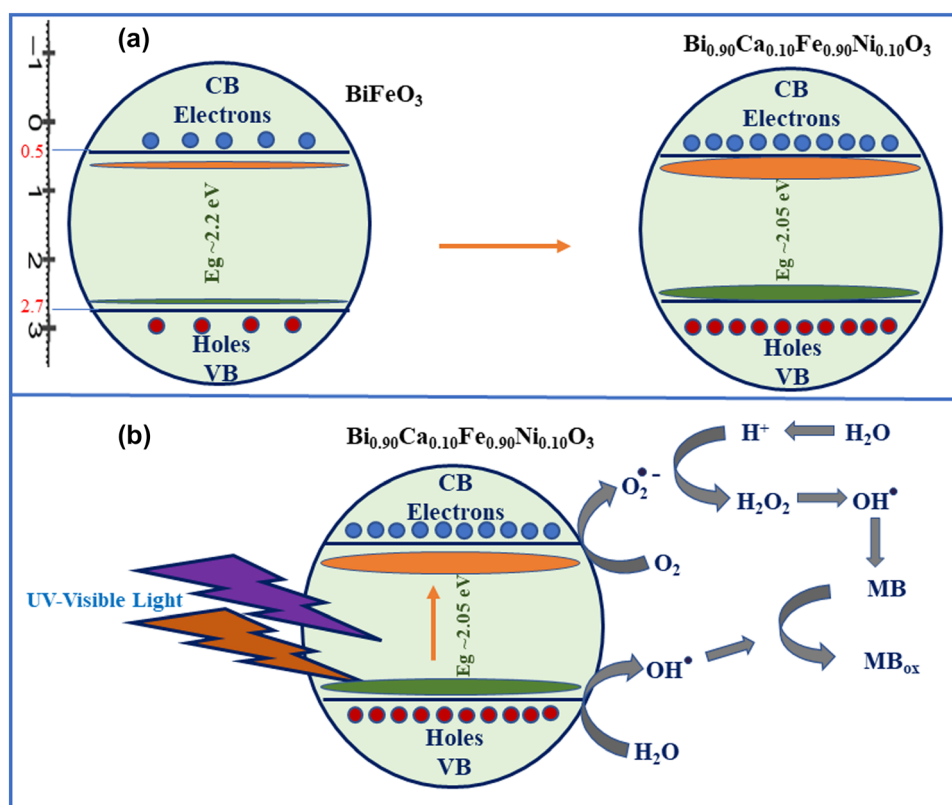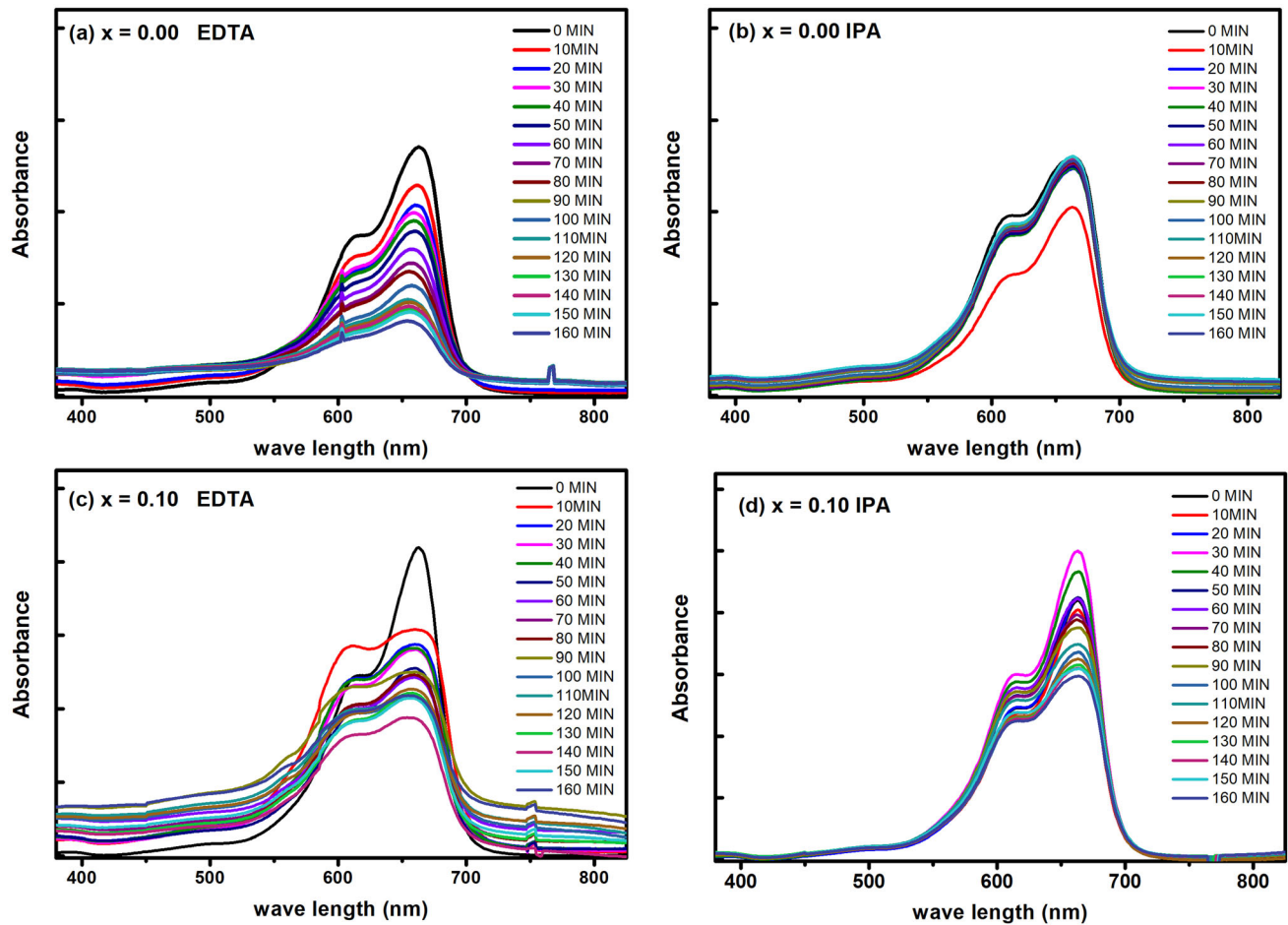
Fig. 12 UV–Visible absorption of MB with different irradiation time in the presence of EDTA and IPA with **a–b** BiFeO$_3$ and **c–d** Bi$_{0.90}$Ca$_{0.10}$Fe$_{0.90}$Ni$_{0.10}$O$_3$ nano-photocatalyst, respectively

trapping reagents; ethylene diamine tetra-acetic acid (EDTA) and Isopropanol (IPA) were used as O$_2^-$ and OH$^-$ trapping reagents, respectively. In 10 ppm MB dye solution, a fixed amount of photocatalyst was added with same amount of scavenger reagents EDTA or IPA [50]. The whole photocatalytic reaction was performed under UV irradiation at constant temperature. The samples were collected after each 10 min intervals and their absorption spectra was found with the help of UV–Visible Spectroscopy as shown in Fig. 12. The absorption graph confirmed that the photocatalytic activity BiFeO$_3$ and

Bi$_{0.90}$Ca$_{0.10}$Fe$_{0.90}$Ni$_{0.10}$O$_3$ catalysts decreased in the existence of EDTA and IPA. The kinetics graphs as shown in Fig. 13) also confirmed that the MB dye degradation rate of BiFeO$_3$ was reduced from 95.2 to 71.33% and 1.41% in the presence of EDTA and IPA, respectively. Similarly, the MB diminishment efficiency for Bi$_{0.90}$Ca$_{0.10}$Fe$_{0.90}$Ni$_{0.10}$O$_3$ catalysts also reduced from 98.38 to 48.68% and 29.2% with EDTA and IPA trapping reagents. The results showed that holes and superoxide oxygen radicals were mainly responsible for MB dye degradation [52, 53].
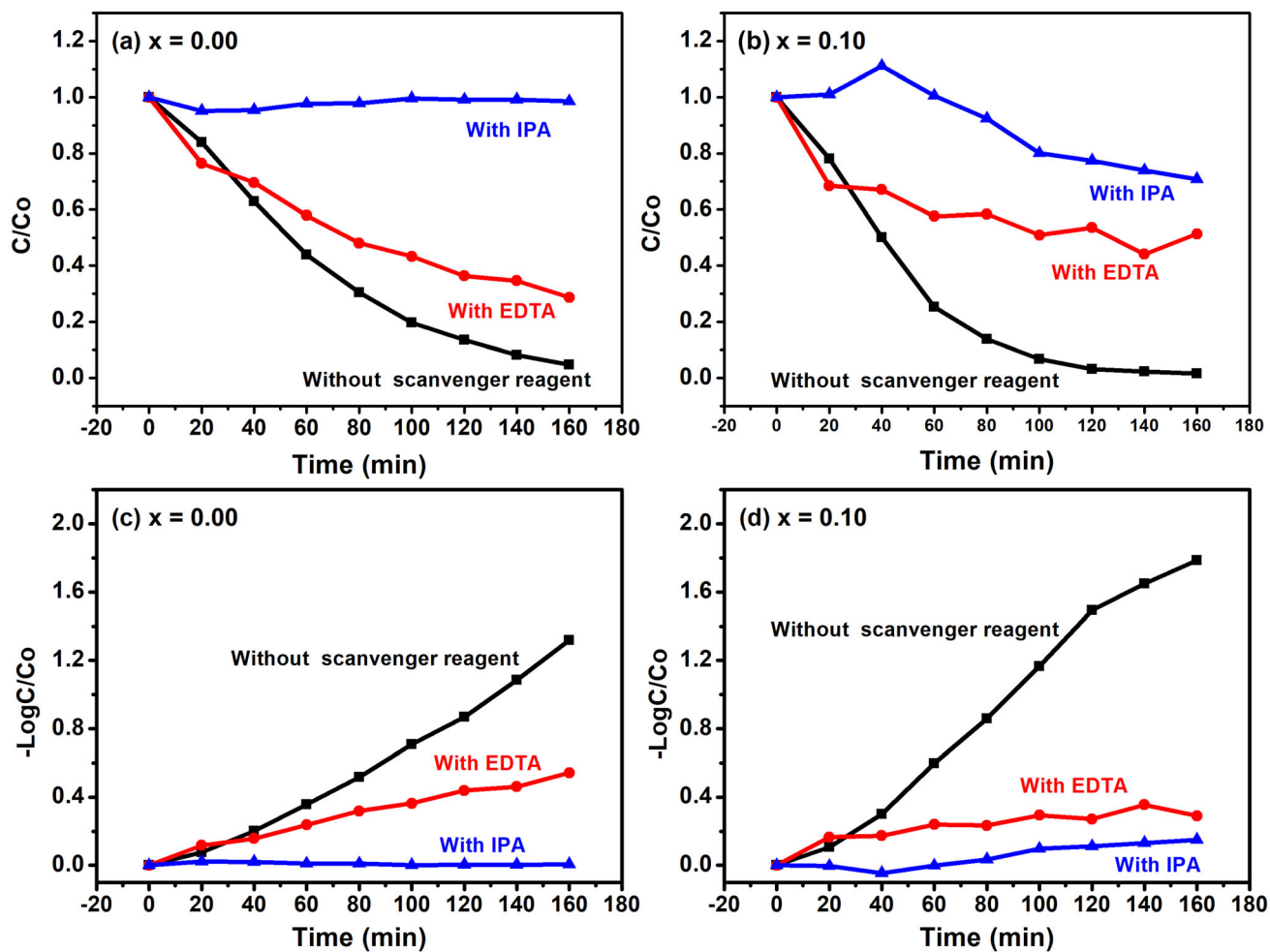
Fig. 13 C/C_0 Vs Time and $-$ Log(C/Co) vs Time of MB degradation in the presence of EDTA and IPA. **a**, **c** for $BiFeO_3$ and **c**, **d** for $Bi_{0.90}Ca_{0.10}Fe_{0.90}Ni_{0.10}O_3$ nano-photocatalyst

4 Conclusion

$Bi_{1-x}Ca_xFe_{1-x}Ni_xO_3$ (x = 0.0, 0.05, 0.10) multiferroic nanoparticles were synthesized by a well-known synthesis method named sol–gel using tartaric acid chelating reagent. Rietveld analysis confirms pure BFO exhibited rhombohedral structure with $R3c$ space, whilst co-doped samples show co-existence of rhombohedral and orthorhombic phases with $R3c$ and $Pnma$ space group, respectively. Raman spectra shows reduction in intensity of E(TO2) mode, gradual enhancement in intensity of A_1(TO1) mode, merging of E(TO2) and A_1(TO1) mode. Additional modes above 400 cm^{-1} involved in changes in magnetic behaviour and these modes are boosted for x = 0.10 samples. Changes in Raman mode's behaviour strongly suggest structural transformation from $R3c$ to another space group $Pnma$. The M–H curve of

pure BFO shows antiferromagnetic (AFM) behaviour with retentivity M_r = 0.005 emu/g and net magnetization M_S = 0.11 emu/g at 15 kOe. Whilst the hysteresis curve of x = 0.05 and 0.10 samples show ferromagnetic behaviour with M_r = 0.0018 emu/g and 0.0078 emu/g and maximum magnetization M_{s-} = 0.37 emu/g and 2.94 emu/g at 15kOe, respectively. XPS result indicates the increase of Fe^{2+} ions with increasing Ca–Ni co-doping. The existence of Fe^{2+} ions contribute significantly in boosting of double exchange interaction between Fe^{2+} and Fe^{3+} ions through oxygen, followed by a drastic change in $BiFeO_3$ magnetic behaviour from antiferromagnetic to ferromagnetic nature on Ca–Ni co-substitution. ESR spectra parameters along with the XPS results confirm the increase of ferromagnetic properties in Ca-Ni substituted samples. UV–visible outcomes specify the energy band gap values reduced after

substituting Ca-Ni in host $BiFeO_3$ from 2.2 to 2.17 eV for $Bi_{0.95}Ca_{0.05}Fe_{0.95}Ni_{0.05}O_3$ and 2.2 eV to 2.05 eV for $Bi_{0.90}Ca_{0.10}Fe_{0.90}Ni_{0.10}O_3$ samples. The photocatalytic result demonstrated that the $Bi_{0.90}Ca_{0.10}Fe_{0.90}Ni_{0.10}O_3$ photocatalyst shows maximum MB dye degradation 98.36% in 160 min irradiation under UV-light. The efficient photodegradation of Ca–Ni substituted $BiFeO_3$ is due to the more photo induced charge separation and reduction of charge recombination rate.

Acknowledgments

Declarations

Conflict of interest The authors declare that they have no known competing financial interests or personal relationships that could have appeared to influence the work reported in this paper. All co-authors have seen and agree with the contents of the manuscript. All co-authors certify that the submission is original work and is not under review at any other publication.

Data availability The datasets generated during and/or analysed during the current study are available from the corresponding author on reasonable request.

Supplementary Information: The online version contains supplementary material available at https://doi.org/10.1007/s10854-022-08555-5.

References

1. N.A. Spaldin, R. Ramesh, Advances in magnetoelectric multiferroics. Nat. Mater. **18**, 203–212 (2019). https://doi.org/10.1038/s41563-018-0275-2

2. J.F. Scott, Applications of magnetoelectrics. J. Mater. Chem. **22**, 4567–4574 (2012). https://doi.org/10.1039/C2JM16137K

3. G. Catalan, J.F. Scott, Physics and applications of bismuth ferrite. Adv. Mater **21**, 2463–2485 (2009). https://doi.org/10.1002/adma.200802849

4. Y. Li, M.-S. Cao, D.-W. Wang, J. Yuan, High-efficiency and dynamic stable electromagnetic wave attenuation for La doped bismuth ferrite at elevated temperature and gigahertz frequency. RSC Adv. **5**, 77184–77191 (2015). https://doi.org/10.1039/C5RA15458H

5. B. Sun, Y. Liu, W. Zhao, P. Chen, Magnetic-field and white-light controlled resistive switching behaviours in Ag/[BiFeO$_3$/ γ Fe$_2$O$_3$]/FTO device. RSC Adv. **5**, 13513–13518 (2015). https://doi.org/10.1039/C4RA14605K

6. S. Das, S. Rana, S. MdMursalin, P. Rana, A. Sen, Sono-chemically prepared nanosized BiFeO$_3$ as novel SO$_2$ sensor. Sens. Actuat. B-Chem. **218**, 122–127 (2015). https://doi.org/10.1021/ac9812429

7. D. Tiwari, D.J. Fermin, T.K. Chaudhuri, A. Ray, Solution processed bismuth ferrite thin films for all-oxide solar photovoltaics. J. Phys. Chem. C **119**, 5872–5877 (2015). https://doi.org/10.1021/jp512821a

8. S. Acharya, S. Martha, P.C. Sahoo, K. Parida, Glimpses towards the modification of perovskite with graphene-analogous materials in photocatalytic applications. Inorg. Chem. Front. **2**, 807–823 (2015). https://doi.org/10.1039/C5QI00124B

9. A. Rogov, M. Irondelle, F. Ramos-Gomez, J. Bode, D. Staedler, S. Passemard, S. Courvoisier, Y. Yamamoto, F. Waharte, D. Ciepielewski, P. Rideau, S. Gerber-Lemaire, F. Alves, J. Salamero, L. Bonacina, J.-P. Wolf, Simultaneous multi-harmonic imaging of nanoparticles in tissues for increased selectivity. ACS Photonics **2**, 1416–1422 (2015). https://doi.org/10.1021/acsphotonics.5b00289

10. F. Mushtaq, X. Chen, M. Hoop, H. Torlakcik, E. Pellicer, J. Sort, C. Gattinoni, B.J. Nelson, S. Pané, Piezoelectrically enhanced photocatalysis with BiFeO$_3$ nanostructures for efficient water remediation. Iscience **4**, 236–246 (2018). https://doi.org/10.1016/j.isci.2018.06.003

11. M.E. Castillo, V.V. Shvartsman, D. Gobeljic, Y. Gao, J. Landers, H. Wende, D.C. Lupascu, Effect of particle size on ferroelectric and magnetic properties of BiFeO$_3$ nanopowders. Nanotechnology **24**, 355701 (2013). https://doi.org/10.1088/0957-4484/24/35/355701

12. T.J. Park, G.C. Papaefthymiou, A.J. Viescas, A.R. Moodenbaugh, S.S. Wong, Size-dependent magnetic properties of single-crystalline multiferroic BiFeO$_3$ nanoparticles. Nano Lett. **7**, 766–772 (2007). https://doi.org/10.1021/nl063039w

13. X. Bai, M. Bugnet, C. Frontera, P. Gemeiner, J. Guillot, D. Lenoble, I.C. Infante, Crystal growth mechanisms of BiFeO$_3$ nanoparticles. Inorg. Chem. **58**(17), 11364–11371 (2019). https://doi.org/10.1021/acs.inorgchem.9b00461

14. P.S.V. Mocherla, C. Karthik, R. Ubic, M.S. Ramachandra Rao, C. Sudakar, Tunable bandgap in BiFeO$_3$ nanoparticles:

the role of microstrain and oxygen defects. Appl. Phys. Lett. **103**, 10220910 (2013). https://doi.org/10.1063/1.4813539

15. P. Suresh, S. Srinath, Effect of synthesis route on the multiferroic properties of BiFeO$_3$: a comparative study between solid state and solgel methods. J. Alloys Compd. **649**, 843–850 (2015). https://doi.org/10.1016/j.jallcom.2015.07.152

16. J.P. Zhou, R.J. Xiao, Y.X. Zhang, Z. Shi, G.Q. Zhu, Novel behaviors of single-crystalline BiFeO$_3$ nanorods hydrothermally synthesized under magnetic field. J. Mater. Chem. **3**, 6924–6931 (2015). https://doi.org/10.1039/C5TC00747J

17. B. Liu, B. Hu, Z. Du, Hydrothermal synthesis and magnetic properties of single-crystalline BiFeO$_3$ nanowires. Chem. Commun. **47**, 8166–8168 (2011). https://doi.org/10.1039/C1CC11896J

18. S. Chauhan, M. Kumar, S. Chhoker, S.C. Katyal, A comparative study on the structural, vibrational, dielectric, magnetic and optical properties of microcrystalline, nanocrystalline BiFeO$_3$ and core-shell structured BiFeO$_3$@-SiO$_2$ nanocomposites. J. Alloy. Compd. **666**, 454–467 (2016). https://doi.org/10.1016/j.jallcom.2016.01.116

19. Q. Zhang, D. Sando, V. Nagarajan, Chemical route derived bismuth ferrite thin films and nanomaterials. J. Mater. Chem. C **4**, 4092–4124 (2016). https://doi.org/10.1039/C6TC00243A

20. D.V. Karpinsky, I.O. Troyanchuk, M.V. Bushinsky et al., Crystal structure and magnetic properties of Bi$_{1-x}$Ca$_x$Fe$_{1-x}$Mn(Ti)$_x$O$_3$ ceramics across the phase boundary. J Mater. Sci. **51**, 10506–10514 (2016). https://doi.org/10.1007/s10853-016-0271-3

21. F. Lin, Q. Yu, L. Deng et al., Effect of La/Cr codoping on structural transformation, leakage, dielectric and magnetic properties of BiFeO$_3$ ceramics. J. Mater. Sci. **52**, 7118–7129 (2017). https://doi.org/10.1007/s10853-017-0947-3

22. S. Bharathkumar, M. Sakar, K. Rohith, S. Balakumar, Versatility of electrospinning on the fabrication of fibrous mat and mesh nanostructures of bismuth ferrite (BiFeO$_3$) and their magnetic, photocatalytic activities. Phys. Chem. Chem. Phys. **17**, 17745–17754 (2015). https://doi.org/10.1039/C5CP01640A

23. X. Yang, G. Xu, Z. Ren, X. Wei, C. Chao, S. Gong, G. Shen, G. Han, The hydrothermal synthesis and formation mechanism of single-crystalline perovskite BiFeO$_3$ microplates with dominant (012) facets. Cry. Eng. Comm. **16**, 4176–4182 (2014). https://doi.org/10.1039/C3CE42488J

24. M.R. Hoffmann, W. Choi, D.W. Bahnemann, Environmental applications of semiconductor photocatalysis. Chem. Rev. **95**, 69–96 (1995). https://doi.org/10.1021/cr00033a004

25. H. Zhou, Y. Qu, T. Zeid, X. Duan, Towards highly efficient photocatalysts using semiconductor nanoarchitectures. Energy Environ. Sci. **5**, 6732–6743 (2012). https://doi.org/10.1039/C2EE03447F

26. P. Caroline, G. Vinitha, D. Joseph, A review on the visible light active BiFeO$_3$ nanostructures as suitable photocatalyst in the degradation of different textile dyes. Environ. Nanotechnol. Monitor. Manag. **7**, 110–120 (2017). https://doi.org/10.1016/j.enmm.2017.02.001

27. F. Gao, X.Y. Chen, K.B. Yin, S. Dong, Z.F. Ren, F. Yuan, T. Yu, Z.G. Zou, J.-M. Liu, Visible-light photocatalytic properties of weak magnetic BiFeO$_3$ nanoparticles. Adv. Mater. **19**, 2889–2892 (2007). https://doi.org/10.1002/adma.200602377

28. J. Kang, Y. Tang, M. Wang, C. Jin, J. Liu, S. Li, Z. Li, J. Zhu, The enhanced peroxymonosulfate-assisted photocatalytic degradation of tetracycline under visible light by g-C$_3$N$_4$/Na-BiVO$_4$ heterojunction catalyst and its mechanism. J. Environ. Chem. Eng. **9**, 105524 (2021). https://doi.org/10.1016/j.jece.2021.105524

29. M. Sakar, S. Balakumar, P. Saravanan, S. Bharathkumar, Compliments of confinements: substitution and dimension induced magnetic origin and bandbending mediated photocatalytic enhancements in Bi$_{1-x}$Dy$_x$FeO$_3$ particulate and fiber nanostructures. Nanoscale **7**, 10667–10679 (2015). https://doi.org/10.1039/C5NR01079A

30. S.M. Selbach, T. Tybell, M.A. Einarsrud, T. Grande, Size-dependent properties of multiferroic BiFeO$_3$ nanoparticles. Chem. Mater. **19**, 6478–6484 (2007). https://doi.org/10.1021/cm071827w

31. K. Fujii, H. Kato, K. Omoto, M. Yashima, J. Chen, X. Xing, Experimental visualization of the Bi–O covalency in ferroelectric bismuth ferrite (BiFeO$_3$) by synchrotron X-ray powder diffraction analysis. Phys. Chem. Chem. Phys. **15**, 6779–6782 (2013). https://doi.org/10.1039/C3CP50236H

32. J.A. Alonso, M.J. Martínez-Lope, J.L. Garcıa-Muñnoz, M.T. Fernández-Díaz, A structural and magnetic study of the defect perovskite LaNiO$_{2.5}$ from high-resolution neutron diffraction data. J. Phys. Condens. Matter **9**, 6417–6426 (1997). https://doi.org/10.1088/0953-8984/9/30/010

33. J. Bielecki, P. Svedlindh, D.T. Tibebu, S. Cai, S.-G. Eriksson, L. Böorjesson, C.S. Knee, Structural and magnetic properties of isovalently substituted multiferroic BiFeO$_3$. Phy. Rev. B **86**, 184422 (2012). https://doi.org/10.1103/PhysRevB.86.184422

34. P. Hermet, M. Goffinet, J. Kreisel, Ph. Ghosez, Raman and infrared spectra of multiferroic bismuth ferrite from first principles. Phys. Rev. B **75**, 220102 (2007). https://doi.org/10.1103/PhysRevB.75.220102

35. H. Feng, The role of Coulomb and exchange interaction on the Dzyaloshinskii-Moriya interaction (DMI) in BiFeO$_3$. J. Mag. Mag. Mater. **322**, 1765–1769 (2010). https://doi.org/10.1016/j.jmmm.2009.12.025

36. S. Chauhan, M. Kumar, S. Chhoker, S.C. Katyal, M. Jewariya, B.N. Suma, G. Kunte, Structural modification and enhanced magnetic properties with two-phonon in Ca-Co codoped BiFeO3 nanoparticles. Ceram. Int. **41**, 14306–14314 (2015). https://doi.org/10.1016/j.ceramint.2015.07.062

37. S. Chauhan, M. Kumar, A. Yousuf, P. Rathi, M. Sahni, S. Singh, Effect of Na/Co co-substituted on structural, magnetic, optical and photocatalytic properties of $BiFeO_3$ nanoparticles. Mater. Chem. Phys. **263**, 124402 (2021). https://doi.org/10.1016/j.matchemphys.2021.124402

38. S. Chauhan, B. Tripathi, M. Kumar, M. Sahni, R.C. Singh, S. Singh, Influence of Na substitution on structural, magnetic, optical and photocatalytic properties of bismuth ferrite nanoparticles. J. Mater. Sci. **31**(22), 20191–20209 (2020). https://doi.org/10.1007/s10854-020-04540-y

39. Z. Quan, W. Liu, H. Hu, S. Xu, B. Sebo, G. Fang, M. Li, X. Zhao, Microstructure, electrical and magnetic properties of Ce-doped $BiFeO_3$ thin films. J. Appl. Phys. **104**, 084106 (2008). https://doi.org/10.1063/1.3000478

40. A. Tamilselvan, S. Balakumar, M. Sakar, C. Nayek, P. Murugavel, K.S. Kumar, Role of oxygen vacancy and Fe–O–Fe bond angle in compositional, magnetic, and dielectric relaxation on Eu-substituted $BiFeO_3$ nanoparticles. Dalton Trans. **43**, 5731–5738 (2014). https://doi.org/10.1039/C3DT52260A

41. R. Pisarev, A. Moskvin, A. Kalashnikova, T. Rasing, Chemical pressure effect on optical properties in multiferroic bulk $BiFeO_3$. Phys. Rev. B **79**, 235128 (2009). https://doi.org/10.1063/1.4757589

42. H. Zhang, W. Liu, P. Wu, X. Hai, M. Guo, X. Xi, J. Gao, X. Wang, F. Guo, X. Xu, C. Wang, G. Liu, W. Chu, S. Wang, Novel behaviors of multiferroic properties in Na-doped $BiFeO_3$ nanoparticles. Nanoscale **6**, 10831–10838 (2014). https://doi.org/10.1039/c4nr02557a

43. S. Chauhan, M. Kumar, H. Pandey, S. Chhoker, S.C. Katyal, Ca–Li substitution driven structural, dynamics of electron density, magnetic and optical properties of $BiFeO_3$ nanoparticles. J. Alloys Compd. **811**, 151965 (2019). https://doi.org/10.1016/j.jallcom.2019.151965

44. Y. Zhang, Y. Yang, Z. Dong, J. Shen, Q. Song, X. Wang, W. Mao, Y. Pu, X. Li, Enhanced photocatalytic activity of Ba doped $BiFeO_3$ by turning morphologies and band gap. J Mater Sci: Mater Electron. **31**, 15007–15012 (2020). https://doi.org/10.1007/s10854-020-04064-5

45. Y. Zhang, Z. Wang, J. Zhu, X. He, H. Xue, S. Li, X.A. Li et al., Ferroelectric polarization effect on the photocatalytic activity of $Bi_{0.9}Ca_{0.1}FeO_3$/CdS S-scheme nanocomposites. J. Environ. Sci. **124**, 310–318 (2022). https://doi.org/10.1016/j.jes.2021.09.021

46. S. Li, Y. Tang, M. Wang, J. Kang, C. Jin, J. Liu, Z. Li, J. Zhu, NiO/g-C_3N_4 2D/2D heterojunction catalyst as efficient peroxymonosulfate activators toward tetracycline degradation: characterization, performance and mechanism. J. Alloy. Compd. **880**, 160547 (2021). https://doi.org/10.1016/j.jallcom.2021.160547

47. Z. Hu, D. Chen, S. Wang, N. Zhang, L. Qin, Y. Huang, Facile synthesis of Sm-doped $BiFeO_3$ nanoparticles for enhanced visible light photocatalytic performance. Mater. Sci. Eng. B **220**, 1–12 (2017). https://doi.org/10.1016/j.mseb.2017.03.005

48. S. Irfan, Y. Shen, S. Rizwan, H.C. Wang, S.B. Khan, C.W. Nan, Band-gap engineering and enhanced photocatalytic activity of Sm and Mn doped $BiFeO_3$ nanoparticles. J. Am. Ceram. Soc. **100**, 31–40 (2017). https://doi.org/10.1111/jace.14487

49. E. Moradi, H. Farajnejad Ghadi, M. Rabbani, R. Rahimi, Microwave-assisted synthesized and characterization of $BiFeO_3$ (CTAB/PEG/PVA) nanocomposites by the auto-combustion method with efficient visible-light photocatalytic dye degradation. J. Mater. Sci. **32**, 8237–8248 (2021). https://doi.org/10.1007/s10854-020-05202-9

50. S. Irfan, L. Li, A.S. Saleemi, C.W. Nan, Enhanced photocatalytic activity of La^{3+} and Se^{4+} co-doped bismuth ferrite nanostructures. J. Mater. Chem. A **5**(22), 11143–11151 (2017). https://doi.org/10.1039/C7TA01847A

51. S.M. Lam, Z.H. Jaffari, J.C. Sin, Hydrothermal synthesis of coral-like palladium-doped $BiFeO_3$ nanocomposites with enhanced photocatalytic and magnetic properties. Mater. Lett. **224**, 1–4 (2018). https://doi.org/10.1016/j.matlet.2018.04.058

52. S. Bharathkumar, M. Sakar, S. Balakumar, Egg white-mediated synthesis of $BiFeO_3$ cubes and their enhanced photocatalytic degradation properties under solar irradiation. J. Mater. Sci. (2022). https://doi.org/10.1007/s10854-022-08213-w

53. A. Indriyani, Y. Yoki, R. Yunarti, D. Apriandanu, S. Rizki, One-pot green fabrication of BiFeO3 nanoparticles via *Abelmoschus esculentus* L. leaves extracts for photocatalytic dye degradation. Appl. Surface Sci. **563**, 150113 (2021). https://doi.org/10.1016/j.apsusc.2021.150113